



Rit Veðurstofu Íslands

*Þóra Árnadóttir
Kim B. Olsen*

*Simulation of surface velocities and
stress changes for the $M_s=7.1$, 1784
earthquake, Iceland*

VÍ-R00003-JA03
Reykjavík
October 2000

ISSN 1025-0565
ISBN 9979-878-18-5

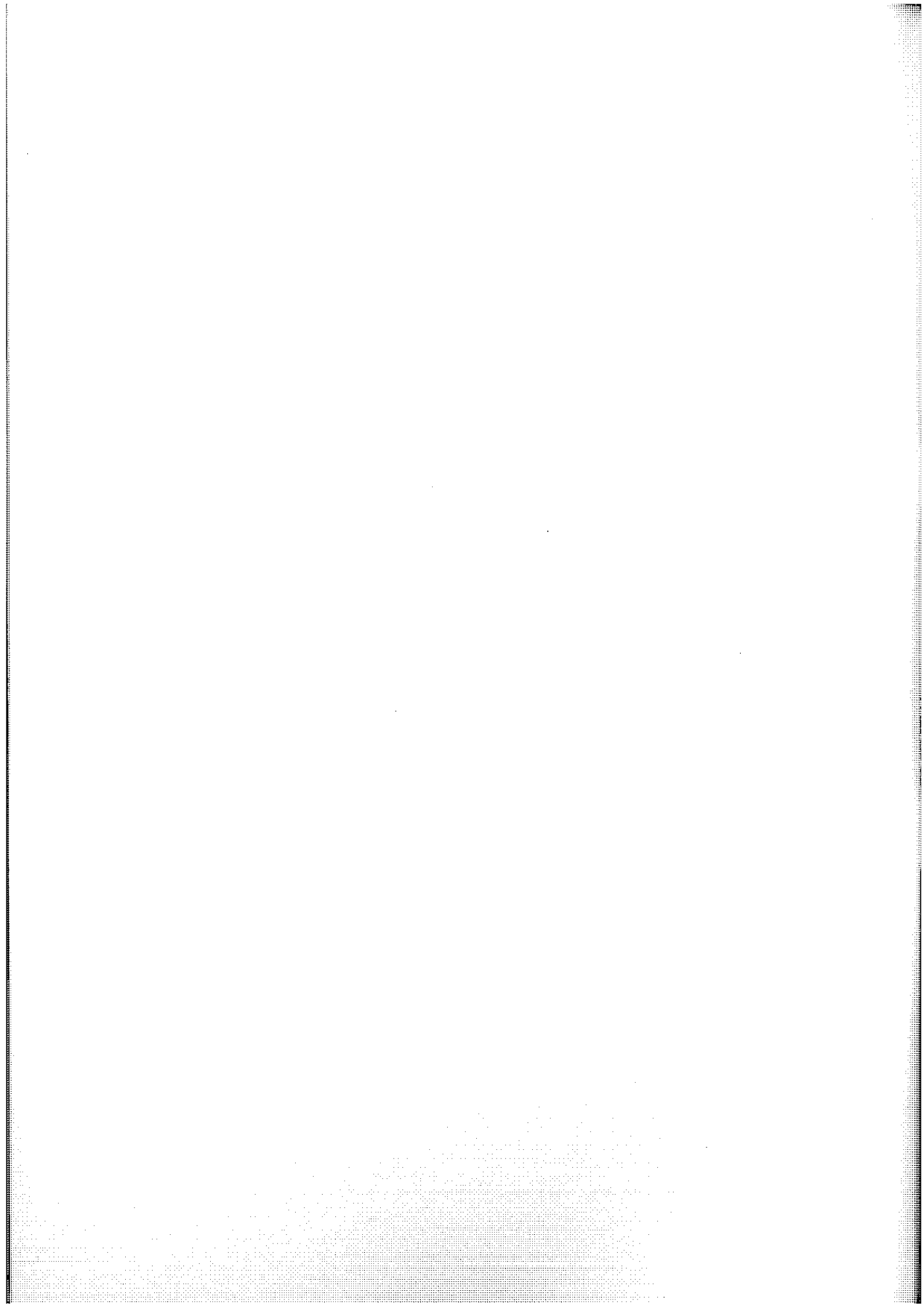
Þóra Árnadóttir
Kim B. Olsen

*Simulation of surface velocities and
stress changes for the $M_S=7.1$, 1784
earthquake, Iceland*

VÍ-R00003-JA03
Reykjavík
October 2000

CONTENTS

1	ABSTRACT	5
2	INTRODUCTION	5
3	MODEL PARAMETERS	8
4	SCENARIOS FOR THE $M_S=7.1$, 1784 EARTHQUAKE	10
5	UNIFORM MOMENT MODELS	10
5.1	Reference model	11
5.2	Effect of vertically-varying crustal structure	15
5.3	Variable rupture velocity	16
6	SLIP DISTRIBUTION	18
7	MAXIMUM FREQUENCY	19
8	WAVE PROPAGATION	21
9	SYNTHETIC SEISMOGRAMS	22
10	COULOMB STRESS CHANGE	22
11	DISCUSSION AND CONCLUSIONS	26
12	ACKNOWLEDGEMENTS	28
13	REFERENCES	30



1 ABSTRACT

We use a finite-difference method to simulate the $M_S=7.1$ earthquake of August 14, 1784, which occurred in the South Iceland seismic zone, believed to have been the largest historical earthquake in Iceland. The August 14 earthquake was followed by a $M_S=6.7$ event on August 16, located approximately 30 km to the west. We first examine the surface velocities generated by a $M_S=7.1$ earthquake in South Iceland. We then calculate the static Coulomb stress changes caused by this earthquake, and determine if it could have triggered the second event. The surface velocities are calculated by simulating a rupture on a N–S, vertical, right-lateral strike-slip fault. We vary the fault geometry, slip distribution, and rupture velocity and compare the peak velocities calculated at the surface obtained for the different models. We find that the simulated peak velocities depend significantly on the depth to the top of the fault. The fault-parallel and vertical peak velocities decrease significantly if the fault does not break the surface, while the fault-perpendicular component is less affected. A model with a heterogeneous slip distribution yields a very different pattern and lower magnitude of surface peak velocities than uniform moment models. This is partly due to the variable slip at shallow depth in the distributed slip model. We calculate the static Coulomb stress change for two models of the August 14, 1784 earthquake. We find that the stress changes caused by the August 14 earthquake are likely to have triggered the August 16 event if the southern end of the rupture was due east of the hypocenter of the second event.

2 INTRODUCTION

Numerous large ($M \geq 6$) earthquakes have occurred in the South Iceland seismic zone (SISZ) since Iceland was settled in the ninth century A.D. The first one to be instrumentally recorded occurred in 1912 in the eastern part of the SISZ and was of $M_S=7.0$ (Bjarnason et al. 1993a). This event has been used to calibrate the size of all previous known historical earthquakes in the area, based on accounts of structural damage (Halldórsson et al. 1984). Estimation of epicenter location of the historical events in the SISZ is also based on accounts of structural damage as well as reports of surface rupture (Halldórsson et al. 1984). The historical earthquake with the largest estimated magnitude, $M_S=7.1$ (Stefánsson et al. 1993), and the focus of our study, occurred on August 14, 1784. Two days later, on August 16, a $M_S=6.7$ earthquake occurred approximately 30 km west of it.

The SISZ is a left-lateral E–W transform zone that connects the Reykjanes peninsula (RP), and the western volcanic zone (WVZ) to the west to the eastern volcanic zone (EVZ) to the east (Figure 1). The N–S orientation of mapped surface faults (Einarsson and Eiríksson 1982) and the N–S elongated zone of destruction for many of the historical earthquakes (Björnsson 1978) suggest that the relative plate motion is accommodated by right-lateral strike-slip faulting on many parallel N–S oriented faults (see Figure 1), rather than a single E–W oriented transform fault. This N–S orientation of faults has also been observed along the Reykjanes peninsula, west of the SISZ (Hreinsdóttir et al. 2000).

There have been sequences of several large earthquakes over a period of days to years, starting with an earthquake in the eastern part of the SISZ and continuing with events further to the west. The time interval between large earthquake sequences in the SISZ ranges between 45 and 112 years (Einarsson et al. 1981). Such series of earthquakes occurred for example in 1630–1633, 1732–1734, 1784, 1896 and 2000.

After the 1912 event, there were no large earthquakes in the SISZ until a $M_S=5.8$ earthquake

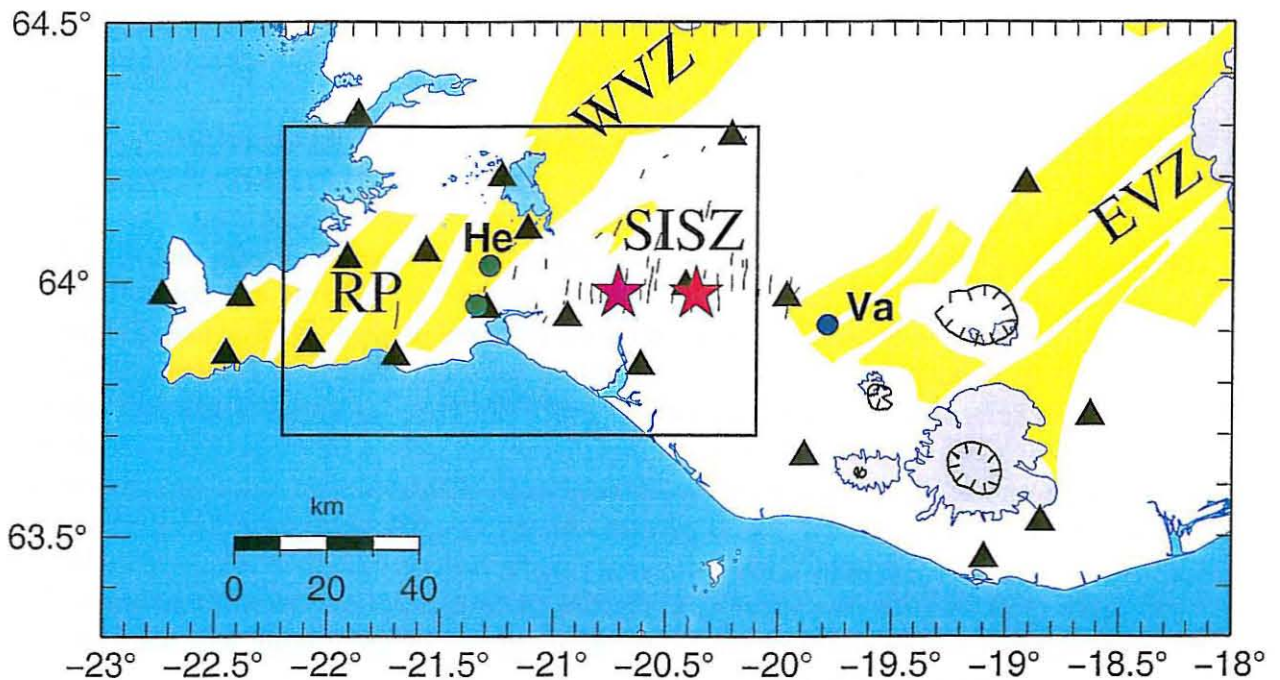


Figure 1. Map of the southwestern part of Iceland. The locations of the $M_S=6.6$, June 17 and June 21, 2000 earthquakes are shown with a red and a purple star, respectively. The June 1998 and November 1998 earthquake epicenters in the Hengill area (He) are shown with green dots. The May 1987 epicenter near Vatnafjöll (Va) is shown with a blue dot. The locations of the South Iceland seismic zone (SISZ), Reykjanes peninsula (RP), western volcanic zone (WVZ) and eastern volcanic zone (EVZ) are shown. The black box shows the extent of the area used in the velocity simulation. Thin black lines denote mapped surface faults (Einarsson and Eiríksson 1982; Einarsson and Sæmundsson 1987; Erlendsson and Einarsson 1996). The yellow areas are volcanic fissure swarms, and the calderas are shown with black lines with tick marks. The locations of SIL seismic stations are shown with black triangles.

occurred in Vatnafjöll in 1987, near the eastern boundary of the SISZ and EVZ. Its epicentral location is shown with a blue dot in Figure 1. Seismic and volumetric strain data used to model the event indicate right-lateral strike-slip on a near vertical fault, with a northerly strike (Bjarnason and Einarsson 1991; Ágústsson et al. 1999). In 1998, two $M_L=5$ earthquakes occurred at the Hengill triple junction, at the western end of the SISZ. Their epicentral locations are shown with green dots in Figure 1. Both events were well recorded on the SIL digital seismic network, which has been operating in Iceland since 1990 (Stefánsson et al. 1993). These events have been modelled using seismic and geodetic data, and appear to have ruptured near vertical, N-S oriented faults with predominantly right-lateral strike-slip motion (Rögnvaldsson et al. 1998; Árnadóttir et al. 1999). The largest earthquakes in the SISZ, since the 1912 event, however, occurred recently at 15:40:41 GMT on June 17 and at 00:51:47 GMT on June 21, 2000. Both these earthquakes have estimated magnitudes of $M_S=6.6$, $M_w=6.5$ and $m_b=5.7-6.1$ (NEIC). The hypocenter of the June 17 event was located at 63.97°N, 20.37°W and 6.3 km depth. The earth-

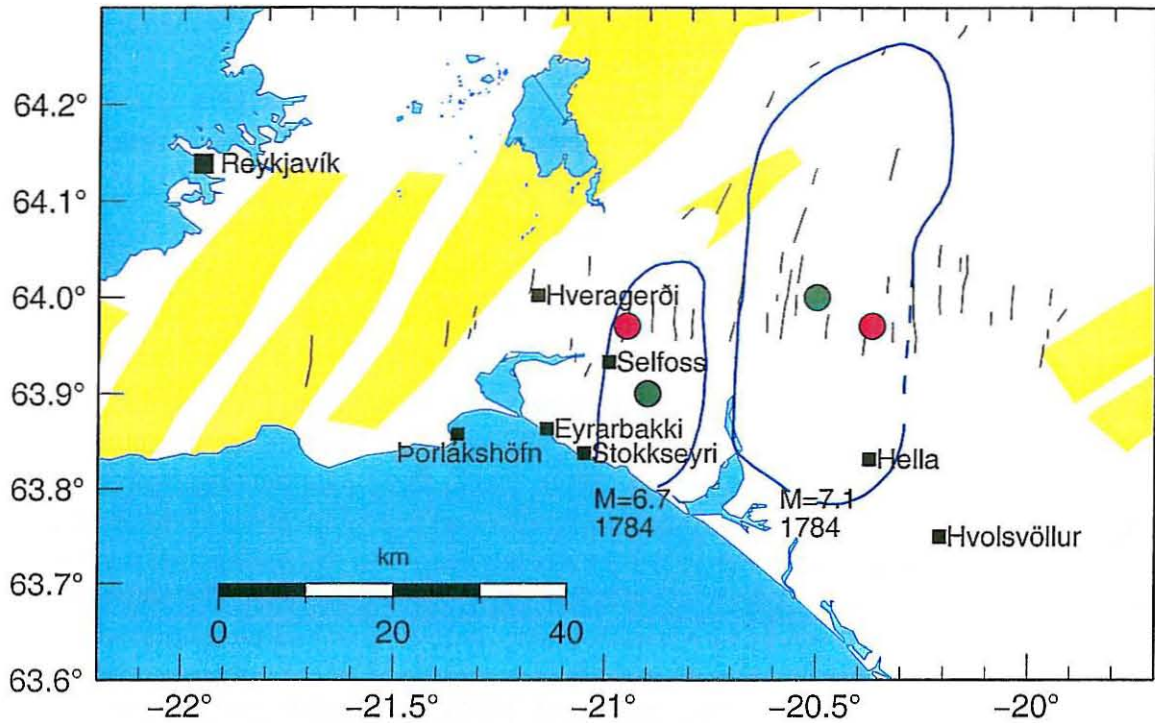


Figure 2. Map of the southwestern part of Iceland. Thin black lines denote mapped faults (Einarsson and Eiríksson 1982; Einarsson and Sæmundsson 1987; Erlendsson and Einarsson 1996). The red dots show estimated epicenters of the $M_S=7.1$ and $M_S=6.7$, 1784 earthquakes, that we use in our study, based on mapped surface faults (P. Einarsson, personal communication, 1999). The green dots show estimated epicenters of the two earthquakes based on areas of destruction (Stefánsson et al. 1993). The regions in which over half of the buildings were destroyed in the earthquakes are shown with N–S elliptical regions drawn in blue (Björnsson 1978). Corresponding intensity is MM VIII–IX (Einarsson et al. 1981). The black squares show current locations of towns and major villages.

quake on June 21 occurred at 63.98°N , 20.71°W and 5.1 km depth. The epicentral locations of the two earthquakes are shown with stars in Figure 1. The aftershocks in their epicentral areas, extended for about 16–18 km N–S, from the surface down to about 10 km depth. The focal mechanisms, determined from teleseismic data, indicate that both earthquakes occurred on N–S oriented faults. Surface faulting was observed for both events, and these indicate rupture on N–S trending faults with left-lateral step-overs (P. Einarsson, personal communication, 2000). The earthquake sequence in June 2000, was recorded by the SIL system, the volumetric strain meter network (Ágústsson et al. 1999), and the continuous GPS network in Iceland (Árnadóttir et al. 2000).

The $M_S=7.1$, August 14, 1784 earthquake caused severe damage in the southern part of Iceland and there are accounts of surface rupture over a large area (Björnsson 1978; Thoroddsen 1899

Parameter	250 m grid	400 m grid
Spatial discretization (km)	0.25	0.4
Temporal discretization (s)	0.015	0.024
Number of E-W grid points	481	320
Number of N-S grid points	319	219
Number of vertical grid points	115	97
Number of time steps	7000	5000
Simulation time (s)	105	120
Maximum frequency resolved (Hz)	1.5	1.0

Table 1. *Parameters for velocity simulations.*

and 1905). The exact epicentral locations of the August 14, $M_S=7.1$, and August 16, $M_S=6.7$, 1784, earthquakes are uncertain. Figure 2 shows the estimated location of the epicenter for the earthquakes based on areas of destruction (green dots) and surface faulting (red dots). We use the locations shown with red dots in our study. The epicentral location of the August 14 earthquake does not greatly affect the velocity calculations, since the map of peak velocities can be shifted further west to match the location shown with the green dot. The outlined areas of destruction correspond to Modified Mercalli intensity of VIII-IX (Einarsson et al. 1981). Recently, a roughly 8 km long N-S surface rupture was mapped in the epicentral area of the $M_S=7.1$ event, using differential GPS (Jónsdóttir et al. 1999). Presumably the fault that ruptured in the earthquake was considerably longer, but traces at the surface are poorly preserved due to the surface geology in the area.

In our study we calculate the velocities and stresses generated by a large earthquake in the SISZ, taking the $M_S=7.1$ earthquake as an example. In our simulations we are concerned with the large-scale effects of a large earthquake in the SISZ, so we consider only simple cases of a single planar rupture. Based on observations of recent events, we assume that the earthquake occurred on a N-S, right-lateral strike-slip fault, at shallow depth. We center our fault model on the estimated epicentral location shown in Figure 2. Since very little is known about the fault geometry, hypocentral depth and location, we run several simulations varying the fault geometry, rupture propagation, slip distribution and analyze the effects these parameters have on the peak ground velocity. The goal is to identify which key parameters are important in estimating reasonable ground velocities in large earthquakes in the SISZ in the future. We also calculate static coseismic stress changes caused by the $M_S=7.1$, August 14 earthquake at the hypocenter of the $M_S=6.7$, August 16 earthquake to examine the possible triggering of the later earthquake by stress changes caused by the larger event. The results from the Coulomb stress calculations are sensitive to the fault locations we use in our study.

3 MODEL PARAMETERS

We use a staggered-grid velocity-stress finite-difference method described by Olsen et al. (1995) to solve the 3D elastic equations of motion (Olsen 1994). The accuracy is fourth-order in space and second-order in time. To limit reflections from the model boundaries we apply absorbing boundary conditions to the sides of the model (Clayton and Engquist 1977), and add a zone of attenuative material (25 nodes) on the sides and bottom of the model (Cerjan et al. 1985). The model parameters for the two grid spacings are shown in Table 1.

The simulation is done for a volume of about 108×67 km horizontally and 28 km vertically. There is no anelastic attenuation in the earth model. The surface velocities we are studying are relatively insensitive to the value of Q (Graves 1998). We use the SIL P- and S-wave velocity model that is used to locate earthquakes in Iceland, based on the refraction measurements of Bjarnason et al. (1993b). The SIL model is shown in Figure 3.

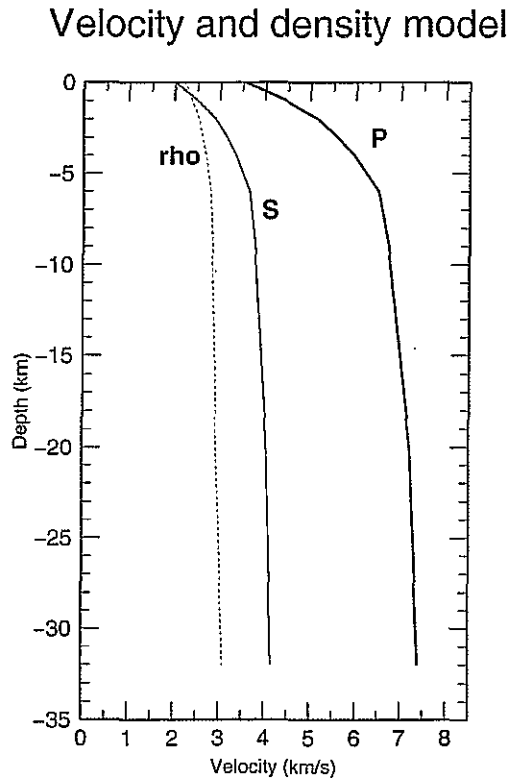


Figure 3. The SIL velocity model and densities for the southwestern part of Iceland. The P- and S-wave velocities are shown in km/s, as a function of depth. The density (ρ) is shown with a dashed line, on the same scale in units g/cm^3 .

The source is described by adding $-M_{ij}(t)/V$ to $S_{ij}(t)$, where M_{ij} is the ij -component of the moment tensor, $V = dx^3$ is the cell volume, and $S_{ij}(t)$ is the ij -component of the stress tensor on the fault at time t . The fault is discretized according to the grid spacing (*i.e.*, 400 m and 250 m). We use an isosceles triangular slip-rate function with an effective rise time of 1.5 s at all the nodes of the fault. The rupture is propagated radially out from the hypocenter at time $t=0$ to the remaining grid points on the fault at a rate of v_r . We test both cases of constant rupture velocity ($v_r=2.7$ km/s) and variable rupture velocity ($v_r=0.85 v_s$). The synthetic seismograms produced are low-pass filtered to 1.0 Hz with a 4-pole Butterworth filter, before calculating the peak velocities. This corresponds to an accuracy of 5 points per minimum S-wave velocity.

Parameter	Value
Longitude of center of fault	20.37°W
Latitude of center of fault	63.97°N
Hypocenter depth†	5, 10 km
Fault length along strike†	20, 50 km
Fault width along dip†	10, 15 km
Fault dip	90°
Fault strike	0°
Rake	180°
Moment ($\times 10^{19}$ Nm)	5.37
Rupture velocity†	2.7 km/s, $0.85v_s$
Rise time	1.5 s

Table 2. *Fault model parameters. Parameters marked with † are varied for different cases.*

4 SCENARIOS FOR THE $M_S=7.1$, 1784 EARTHQUAKE

Based on mapped surface faults and information from recent earthquakes in the SISZ, we simulate the $M_S=7.1$, 1784 earthquake as a bilateral, purely right-lateral strike-slip rupture on a N–S oriented vertical fault plane. The fault parameters are listed in Table 2.

We vary some of the fault parameters (fault length and width, hypocentral depth and location) as well as the slip distribution, to evaluate their effect on the surface velocities. We examine the end member cases of a short fault (20 km long) and a long fault (50 km long). It is likely that the earthquake ruptured a 30–40 km long fault. The estimated thickness of the brittle crust in the SISZ varies from about 5 km at the western end to about 12–15 km at the eastern end (Stefánsson et al. 1993; Tryggvason et al. 2000). In our calculations we consider faults extending vertically down to 10 and 15 km. There is no empirical formula relating the surface wave magnitude, M_S , and seismic moment, M_0 , in the SISZ. A general formula is $\log(M_0) = 1.5M_S + 16.1$, e.g., Lay and Wallace (1995), which gives $M_0 = 5.62 \times 10^{19}$ Nm. An empirical formula derived for Iceland, relating the local magnitude, M_L , and the seismic moment, is given by $\log(M_0) = 10.5 + 1.3M_L$ (Ágústsson et al. 1999). Using this relation we obtain a value of $M_0 = 5.37 \times 10^{19}$ Nm, which we use for the models in our simulations.

In the following sections we compare the calculated three-dimensional peak velocities at the free surface for several different models. We start with the simplest case of uniform moment and use that as our reference model and explore the effect of varying fault geometry and hypocenter location. We then allow the rupture velocity to vary and compare cases of variable fault depth to the reference case. We examine the effect of heterogeneous slip distribution on the fault, and finally increase the maximum frequency to 1.5 Hz by decreasing the grid spacing.

5 UNIFORM MOMENT MODELS

The moment for each subfault (ij) is $M_{ij} = M_0/N$, where M_0 is the total seismic moment and N is the number of subfaults. M_{ij} is therefore constant for each subfault. The slip on each subfault, s_{ij} , is calculated from the moment of each subfault, using the relation $M_{ij} = \mu(z)As_{ij}$. The shear modulus is, $\mu(z) = \rho v_s^2$, where v_s is the S-wave velocity and ρ is density, both of which increase with depth. The slip is therefore not constant over the fault, but decreases with depth. We refer to these models as uniform moment models, since the slip is not uniform on the

fault, although they are often called uniform slip models in the literature. If the earth model is a homogeneous half-space, uniform moment implies uniform slip.

5.1 Reference model

Our reference model is a planar 50 km long, N–S oriented, vertical fault, extending from the free surface down to 15 km depth. The average motion on the fault is about 2.5 m of right-lateral strike-slip. The hypocenter is at the center of the fault at 10 km depth. The fault rupture propagates radially out from the hypocenter with a constant rupture velocity of 2.7 km/s. The rupture propagates from the hypocenter to the ends of the fault in about 9 s.

Figure 4 shows a map view of the calculated peak velocities at the free surface for this model. The top panel shows the E–W component, the center panel shows the N–S component, and the bottom panel shows the vertical component. The maximum peak velocity is 3.9 m/s in the E–W direction, 2.9 m/s in N–S direction and 1.0 m/s in the vertical direction. The color scale extends from 0 m/s (dark blue) to 2.0 m/s (red). The squares show the locations of towns and major villages in the area (see also Figure 2). The surface projection of the fault is shown with a straight line along N–S. We also show the outlines of the area of destruction in the $M_S=7.1$, 1784 earthquake. The largest N–S and vertical peak velocities lie within that area. The maximum peak velocities occur in the E–W direction, because of rupture directivity effects in which the amplitudes of the SH waves increase in the direction of rupture propagation (*e.g.*, Lay and Wallace 1995). The patterns of the peak velocities are symmetric about the fault trace, both along and perpendicular to strike, for all the velocity components, as expected for a bilateral rupture starting at the center of the fault. The fault-parallel component (N–S) shows fairly large peak velocities out to several tens of kilometers away from the fault.

The coherency of long-period radiation is maximized in uniform moment models, generating extremely large motions. In order to compare our reference model with other models, we normalize the surface peak velocities by the maximum value for the corresponding component, *i.e.*, 3.9 m/s for E–W, 2.9 m/s for N–S and 1.0 m/s for the vertical component, respectively. Figure 5 shows the normalized peak velocities for our reference model. The color scale extends from 0 (dark blue) to 1.0 (red). In subsequent plots the peak velocities for the different models are normalized by the same values.

Figure 6 shows the same as Figure 5 for the same model parameters, except the hypocentral depth is now 5 km rather than 10 km. Decreasing the hypocentral depth concentrates the large peak velocities near the fault trace at the center of the fault, for the fault-parallel and vertical components, and at the ends of the fault for the horizontal component. The maximum value of the vertical and fault-parallel components of the peak velocity decreases slightly as the hypocentral depth decreases, whereas the maximum value of the fault-perpendicular component increases.

Figure 7 shows the same as Figure 5 for the same model parameters, except the down-dip fault width is 10 km rather than 15 km. The hypocenter is located at the center of the fault at 5 km depth. A narrow fault increases the peak velocities significantly near the fault. This is understandable because the moment and slip on each subfault increases, when the fault area decreases. The average slip for this model is about 4 m. The overall effect of a narrow fault model is to increase all components of the surface peak velocity near the fault.

Figure 8 shows the same as Figure 5 for the same model parameters, except the fault length is

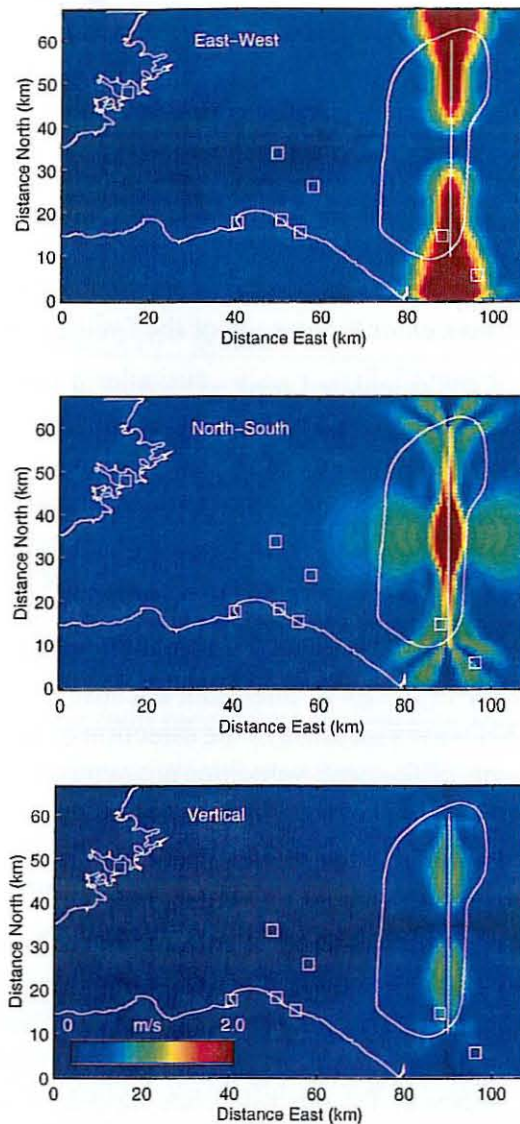


Figure 4. Peak velocity maps for the reference model with 400 m grid spacing. The fault is 50 km long and extends from the surface down to 15 km depth. The slip is uniform right-lateral strike-slip. The hypocenter is in the center of the fault at 10 km depth. The rupture propagates radially out from the hypocenter with a constant rupture velocity of 2.7 km/s. The N-S line shows the surface trace of the fault model. The squares depict current locations of towns and major villages shown in Figure 2. The N-S elongated area corresponding to MM VIII-IX is also shown. The color scale extends from 0 m/s (dark blue) to 2.0 m/s (red). The top panel shows the E-W component, the center panel shows the N-S component, and the bottom panel shows the vertical component.

20 km rather than 50 km. The average slip for this model is about 5 m. A short fault produces higher peak velocities than a long fault, because again the moment and slip on each subfault increase when the fault area decreases. The peak velocities of the fault-parallel component are also significantly larger away from the short fault. The maximum value is in the fault-parallel

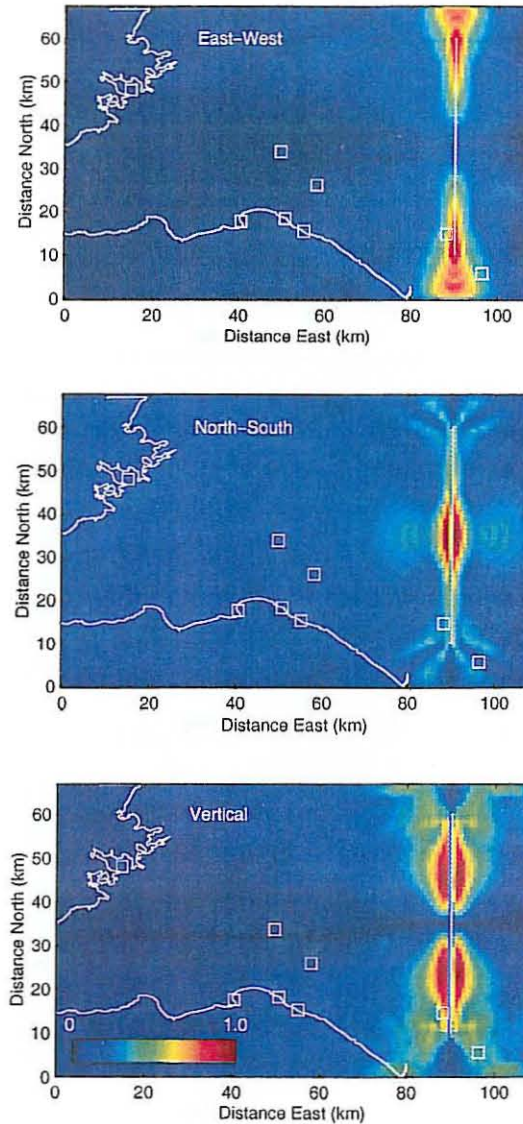


Figure 5. Normalized peak velocities for the same model as shown in Figure 4. Each component of the peak velocity has been divided by the maximum peak velocity for that component. The color scale extends from 0 (dark blue) to 1.0 (red).

direction, as opposed to the fault perpendicular direction found for the 50 km long fault. This is due to the different aspect ratio for this fault model, *i.e.*, it is almost equal in length and width. The other peak velocity components are less amplified.

Figure 9 shows the same as Figure 8 for the same model parameters, except the fault extends down to 10 km rather than 15 km, and the hypocentral depth is 5 km rather than 10 km. Decreasing the fault area further increases the peak velocities, as the slip and moment for each subfault scale inversely with the size of the fault, when we assume a constant moment for the whole fault. The average slip for this model is about 10 m. Comparing Figures 5 and 9 shows that for the same magnitude of the earthquake, decreasing the fault area increases the peak velocities for all components. As we decrease the area of the fault, we approach a point source, and the N-S velocity component approaches a S-wave radiation pattern, while the vertical component

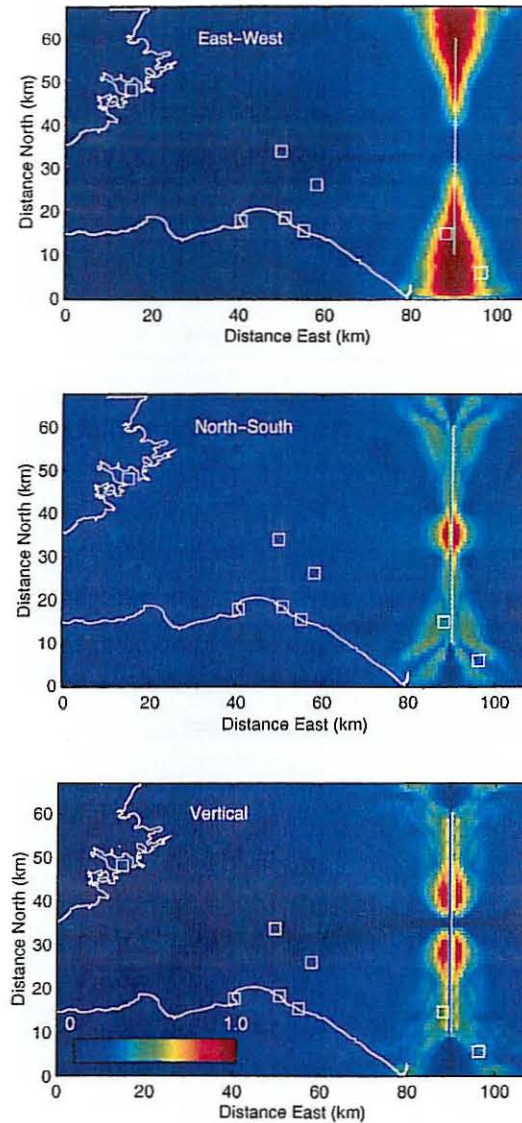


Figure 6. *Normalized peak velocities for a model with 400 m grid spacing and uniform moment. The fault is 50 km long and extends from the surface down to 15 km depth. The hypocenter is in the center of the fault at 5 km depth.*

takes on a P-wave radiation pattern.

Figure 10 shows the same as Figure 5 for the same model parameters, except the hypocenter is now near the southern end of the fault. The rupture is therefore almost unilateral. The pattern of peak velocities is shifted towards the hypocenter and broadens toward the north, particularly the horizontal components. This model shows clearly the effect of rupture directivity on the calculated velocities, which amplifies the fault-perpendicular component. The rupture propagates from south to north, starting at the southern end of the fault. In this case, the peak velocities are lower to the south of the epicenter and larger at the northern end, compared to the scenario where the rupture starts in the center of the fault.

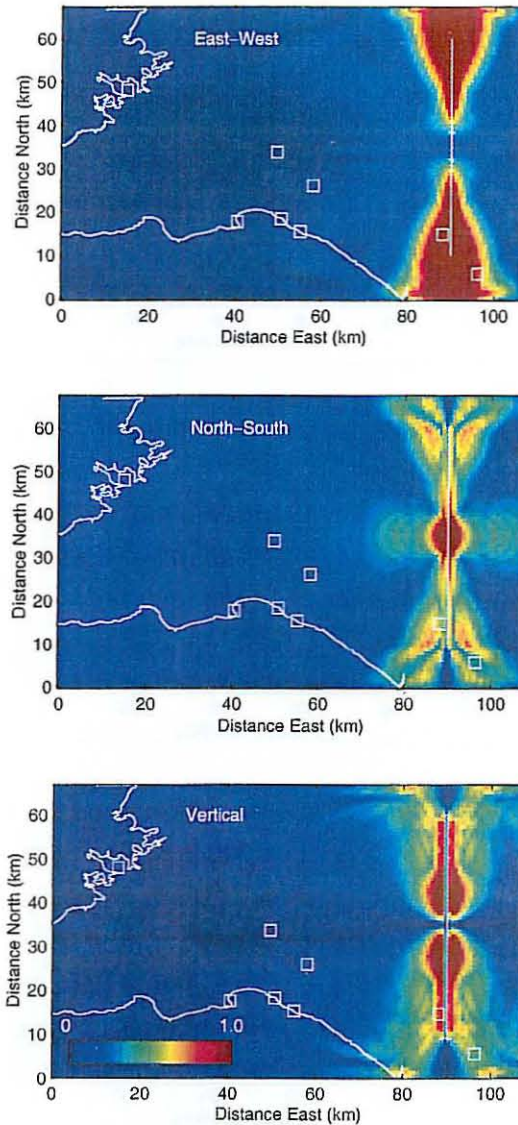


Figure 7. Normalized peak velocities for a model with 400 m grid spacing and uniform moment. The fault is 50 km long and extends from the surface down to 10 km depth. The hypocenter is in the center of the fault at 5 km depth.

5.2 Effect of vertically-varying crustal structure

We examined the effect of vertically-varying crustal structure by comparing our reference model to a half space model with constant v_p and v_s velocities. This model has a constant right-lateral strike-slip of 2.4 m. The fault is 50 km long and extends from the surface down to 15 km depth. Figure 11 shows the normalized peak velocities for the half space model. The model produces relatively small surface peak velocities compared to those for the layered model. This can be explained by the low v_p and v_s velocities near the surface in the layered model effectively trapping P- and S-waves.

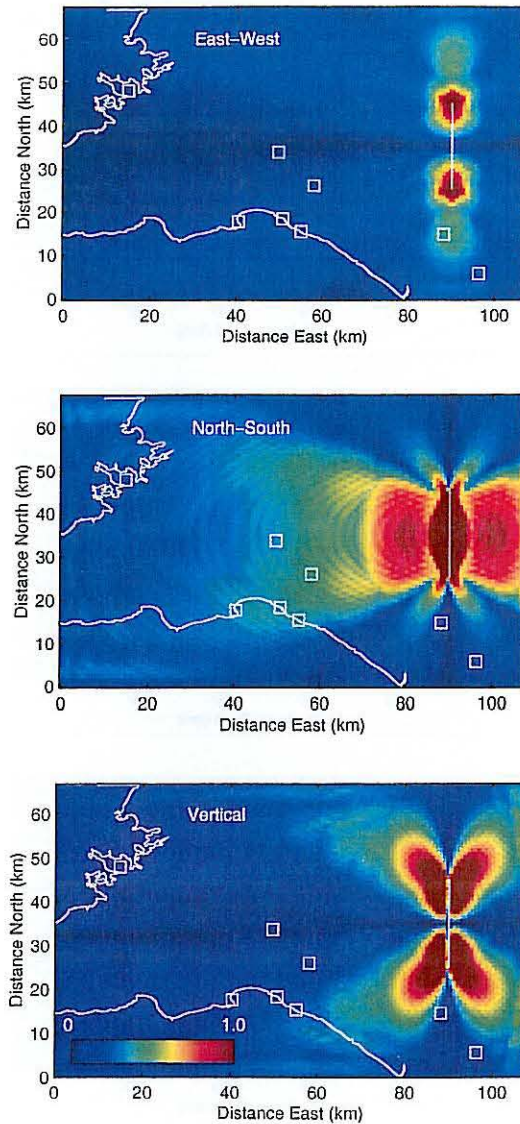


Figure 8. *Normalized peak velocities for a model with 400 m grid spacing and uniform moment. The fault is 20 km long and extends from the surface down to 15 km depth. The hypocenter is in the center of the fault at 10 km depth.*

5.3 Variable rupture velocity

We examined the effect of allowing the rupture velocity (v_r) to vary, rather than keeping it fixed at 2.7 km/s. Figure 12 shows the same as Figure 5, except the rupture velocity is now $v_r = 0.85 v_s$. Note that the rupture velocity decreases as we approach the surface, since it is a fraction of the S-wave velocity. Comparing Figures 12 and 5 we see that the maximum peak velocities are smaller for the variable rupture velocity model than for our reference model, particularly the fault-perpendicular component. This is caused by a decreased coherence of the rupture propagation.

We then examine a model with variable rupture velocity, where the top of fault does not reach the surface, but is buried at 4 km depth, and the fault extends down to 15 km. As before, when

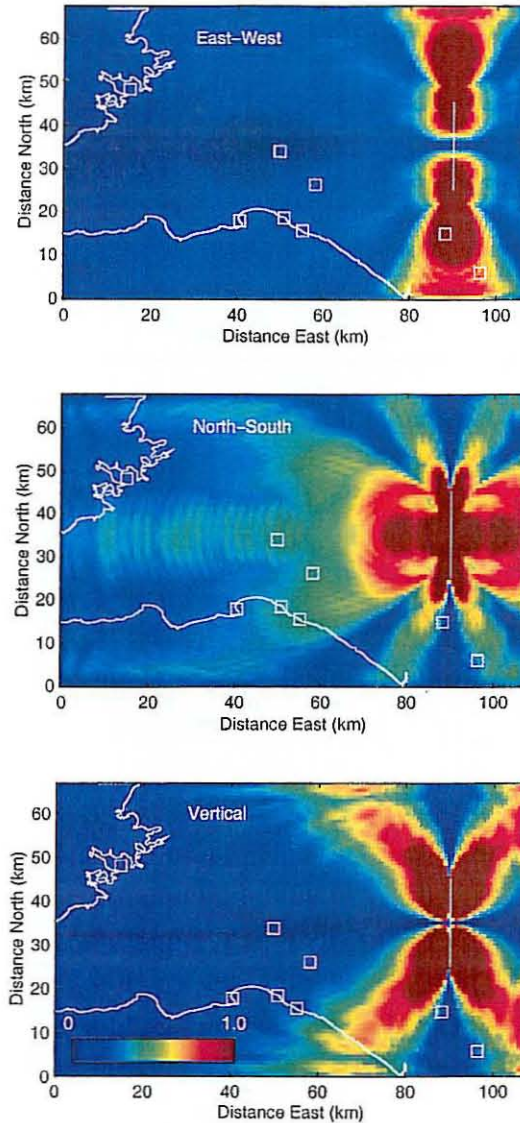


Figure 9. *Normalized peak velocities for a model with 400 m grid spacing and uniform moment. The fault is 20 km long and extends from the surface down to 10 km depth. The hypocenter is in the center of the fault at 5 km depth.*

decreasing the area of the fault, the slip and moment of each subfault increases. Figure 13 shows the normalized surface peak velocities for this case. A comparison of Figures 13 and 12 shows that the peak velocities decrease significantly if the fault does not reach the surface, particularly for the fault-parallel and vertical components of motion. The change in the fault-perpendicular component is less significant.

A fault that reaches the surface produces higher peak velocities at the surface than a buried fault. The rupture velocity effects the peak velocities, but is less critical than the depth of rupture. As mentioned earlier, the constant slip models produce large peak velocities in the near-source region if there are low-velocity layers present. If the fault does not rupture to the surface these shallow low-velocity layers are less important.

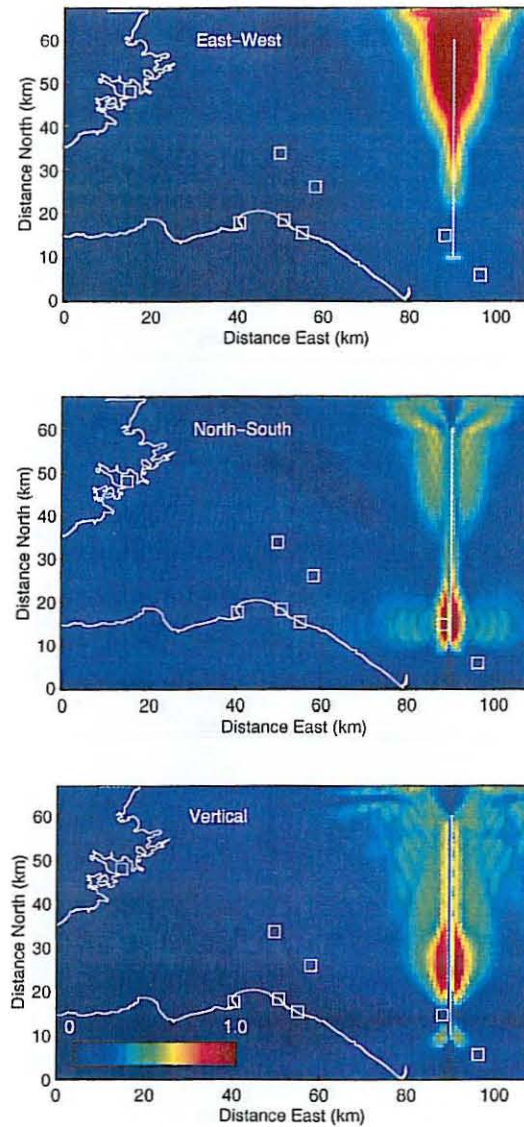


Figure 10. *Normalized peak velocities for a model with 400 m grid spacing and uniform moment. The fault is 50 km long and extends from the surface down to 15 km depth. The hypocenter is near the southern end of the fault at 10 km depth.*

6 SLIP DISTRIBUTION

We now examine how a heterogeneous slip distribution affects the surface peak velocities. We use a scaled version of the slip model estimated for the 1992 $M=7.2$ Landers earthquake (Wald and Heaton 1994), on a 400 m grid. The slip on each subfault is scaled such that the seismic moment of the entire fault is equal to 5.37×10^{19} Nm. The moment is therefore not constant on each subfault as it is in the uniform moment models. Figure 14 shows the slip distribution model. The slip ranges from 0 m (dark blue) to 4.5 m (dark red). The fault is 50 km long, extending vertically from the surface down to 15 km depth. The rupture starts at the center of the fault at 10 km depth and propagates bilaterally from the hypocenter, with a constant velocity. The calculated surface peak velocities for this model are shown in Figure 15. In general, the

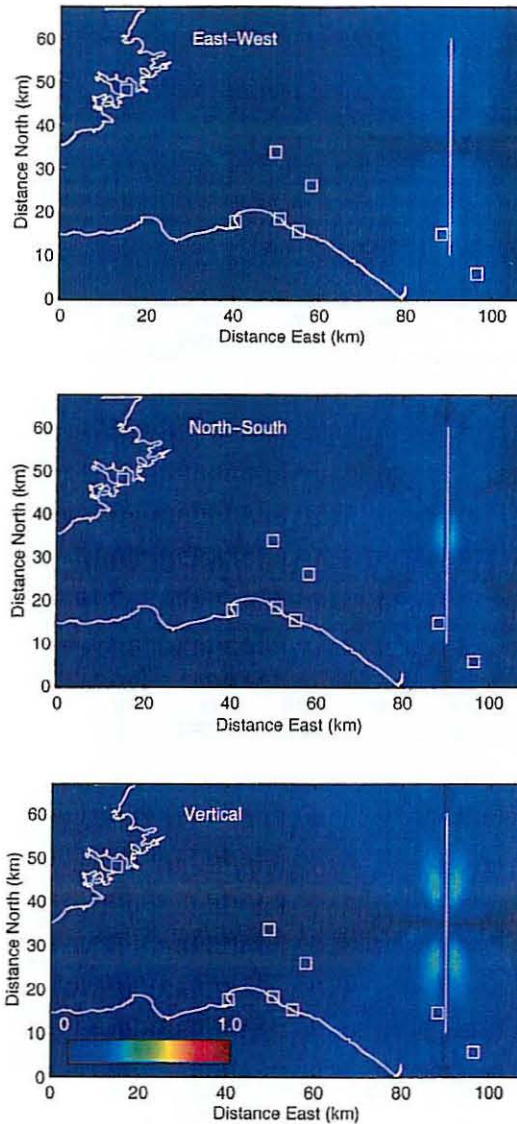


Figure 11. Normalized peak velocities for a half space model with 400 m grid spacing and uniform moment. The fault is 50 km long and extends from the surface down to 15 km depth. The hypocenter is at the center of the fault at 10 km depth.

largest peak velocities correspond to areas of large slip in the model. We see that the peak velocities for the variable slip case are much smaller compared to those for the uniform moment case for all components of motion (Figure 5), in particular the fault-parallel component. The heterogeneous slip model has less moment on each subfault at shallow depth than our reference model, which may account for part of the difference.

7 MAXIMUM FREQUENCY

The grid spacing is an important factor in these simulations, as smaller grid spacing allows higher maximum frequencies (f_m). A model with a 250 m grid spacing allows simulation of $f_m \sim 1.5$ Hz, whereas a 400 m grid is limited to $f_m \sim 1.0$ Hz, for our velocity model, assuming

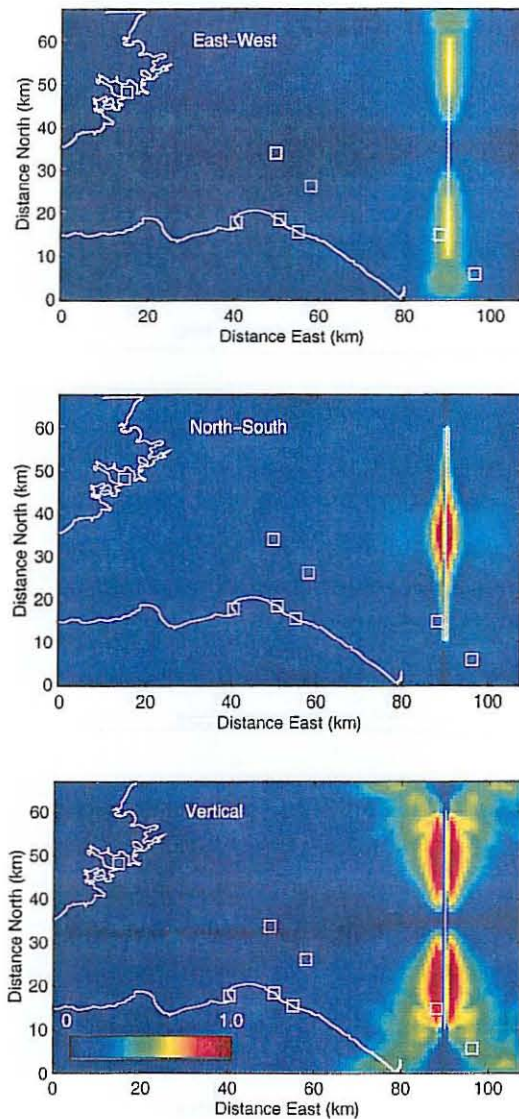


Figure 12. Normalized peak velocities for a model with 400 m grid spacing and uniform moment. The fault is 50 km long and extends from the surface down to 15 km depth. The hypocenter is in the center of the fault at 10 km depth. The rupture velocity is $v_r = 0.85v_s$.

at least 5 points per minimum wavelength. The computation time increases as 2^{16} when the grid spacing is decreased by a factor of 2 for a uniformly gridded model.

Figure 16 shows the normalized 1.5 Hz peak velocities for the reference model, with finer grid spacing (250 m rather than 400 m). The 1.5 Hz simulation increases the peak velocities by up to a factor of 1.5 while the overall pattern seen in Figures 16 and 5 is similar, *i.e.*, the maximum peak velocities are in the fault-perpendicular (E–W) direction.

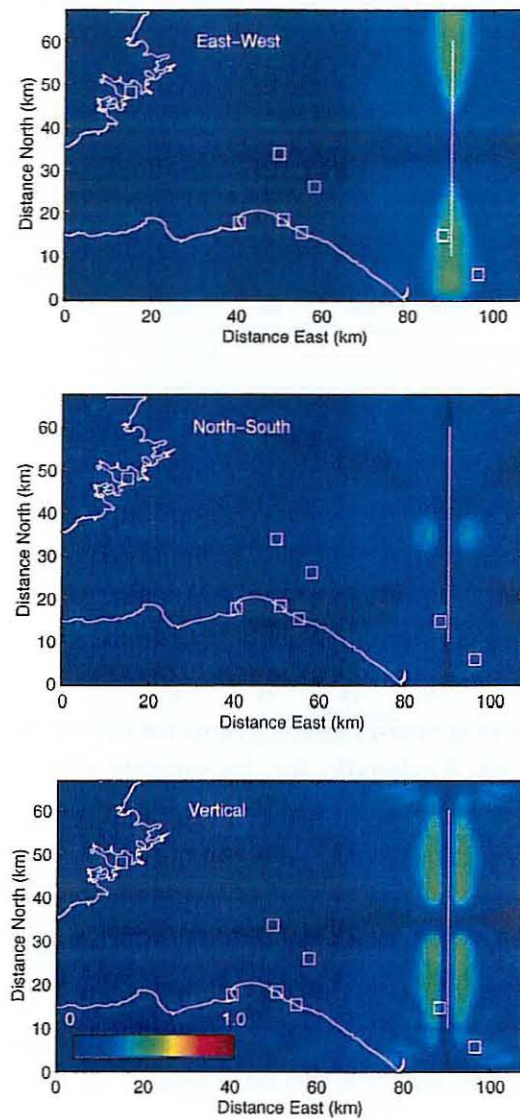


Figure 13. Normalized peak velocities for a model with 400 m grid spacing and uniform motion. The fault is 50 km long and extends from 4 km depth down to 15 km depth. The hypocenter is in the center of the fault at 10 km depth. The rupture velocity is $v_r = 0.85v_s$.

8 WAVE PROPAGATION

Figure 17 shows snapshots of the velocity field for the reference model at times $t = 4.8, 9.6, 12.0, 18.0,$ and 24.0 s. The left panels show the fault-perpendicular component (E–W), the center panels show the fault-parallel component (N–S), and the panels on the right show the vertical component. Red is positive and blue is negative velocity. The rupture has propagated to the ends of the fault at time $t \sim 9$ s and the S-waves have reached Reykjavík at 24 s. We clearly see the propagation of S- and Love-waves in the plots for the fault-parallel component. The S-waves are the first band of yellow color propagating west, out from the fault, followed by larger amplitude Love-waves.

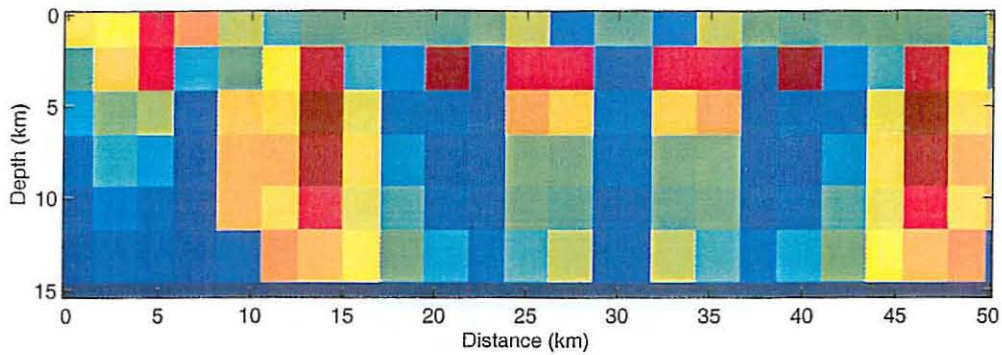


Figure 14. Slip distribution along the fault used to calculate peak velocities for 400 m grid spacing. The fault is 50 km long and extends from the surface down to 15 km depth. The southern end of the fault is at 0 km. The colors show the amount of slip from 0 m (dark blue) to 4.5 m (dark red). The magnitude of the slip in each patch is scaled such that the total moment for the earthquake is 5.37×10^{19} Nm.

9 SYNTHETIC SEISMOGRAMS

Figure 18 shows low-pass filtered synthetic seismograms for the village of Hella, town of Hveragerði, and the capital of Iceland, Reykjavík, for the variable slip model shown in Figure 14. Hella is near the southern end of the fault, Hveragerði is about 40 km to the west and Reykjavík is about 70 km northwest of the fault center. Their locations are shown in Figure 2. We plot the velocities, v , where the subscripts x , y and z , are E–W, N–S and vertical direction, respectively, as a function of time. The velocities are in m/s and time is in seconds. The highest surface velocities are observed at Hella which is in the near field. The maximum velocity at Hella is in the fault-perpendicular direction (E–W). The maximum surface velocities at Hveragerði and Reykjavík are in the fault-parallel direction (N–S). Note that the velocity scale in Figure 18 for Hella is larger than the scale for Hveragerði and Reykjavík.

10 COULOMB STRESS CHANGE

The $M_S=7.1$ August 14, 1784 earthquake was followed two days later by a $M_S=6.7$ earthquake about 30 km to the west of the August 14 epicenter (see Figure 2). In this section we calculate the static coseismic change in Coulomb failure stress caused by the first earthquake to determine whether it is likely to have triggered the second one. We use the same fault parameters as in our reference model, *i.e.*, a vertical, right-lateral strike-slip fault, extending from the surface down to 15 km depth. The fault is embedded in an elastic half-space. We assume a constant slip over the fault and a seismic moment of 5.37×10^{19} Nm. We compare two cases of a 50 km long fault (the slip is then 2.4 m) and a 20 km long fault (with 6.0 m of slip). We assume that both earthquakes were right-lateral strike-slip events on N–S oriented, vertical faults, and that the hypocenter of the second event was at 5 km depth.

We calculate the change in Coulomb failure stress ($\Delta\sigma_{CFS}$) (Harris 1998; Stein 1999), using

$$\Delta\sigma_{CFS} = \Delta\tau_{slip} + \mu' \Delta\sigma_n \quad (1)$$

where $\Delta\tau_{slip}$ is the change in shear stress resolved in the slip direction of the second earthquake (*i.e.*, for these two earthquakes $\Delta\tau_{slip} = \Delta\tau_{xy}$), and $\Delta\sigma_n$ is the change in normal stress due

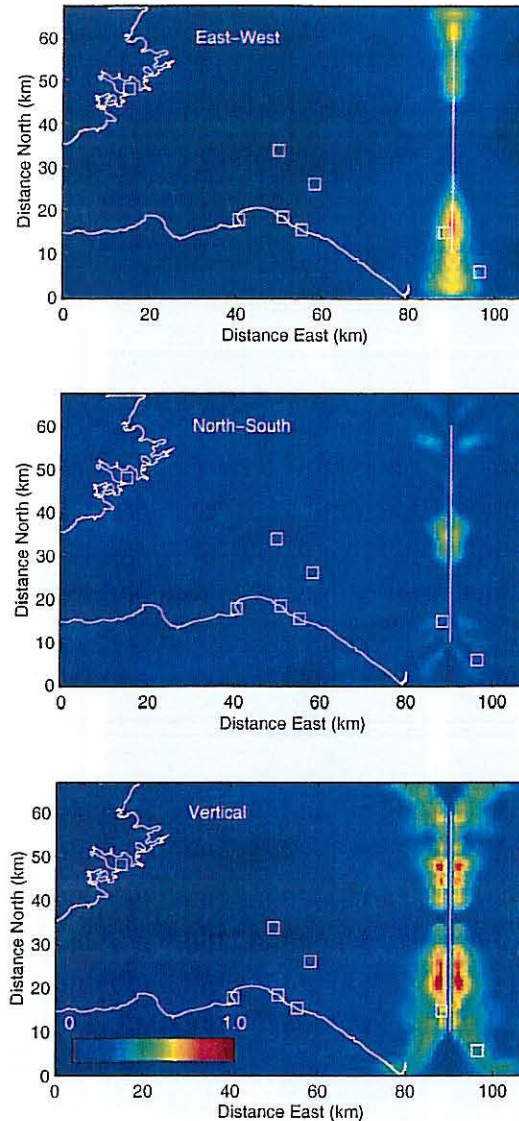


Figure 15. Normalized peak velocities for a model with 400 m grid spacing and variable slip distribution. The fault is 50 km long and extends from the surface down to 15 km depth. The rupture starts at the center of the fault at 10 km depth. The rupture velocity is 2.7 km/s.

to the first earthquake, perpendicular to the second fault plane (here $\Delta\sigma_n = -\Delta\sigma_{xx}$). Positive $\Delta\sigma_n$ implies increased tension, hence the negative sign of $\Delta\sigma_{xx}$. The “apparent coefficient of friction”, μ' , ranges typically from 0 to 0.6 (Harris 1998). We use a value of $\mu'=0.4$, *i.e.*, corresponding to a medium strength fault (King et al. 1994). A positive $\Delta\sigma_{CFS}$ implies an increase in Coulomb failure stress, indicating that the first earthquake brought the second fault closer to failure. It has been suggested that changes in CFS on the order of 0.1 bar affect locations of aftershocks (Harris 1998). We have not included the effects of a local stress field in our calculations.

Figure 19 shows the $\Delta\sigma_{CFS}$ for a 50 km long fault model and Figure 20 shows the same for a 20 km long fault. For the case of a 50 km long fault, we estimate a $\Delta\sigma_{CFS}$ of -0.68 bars at the

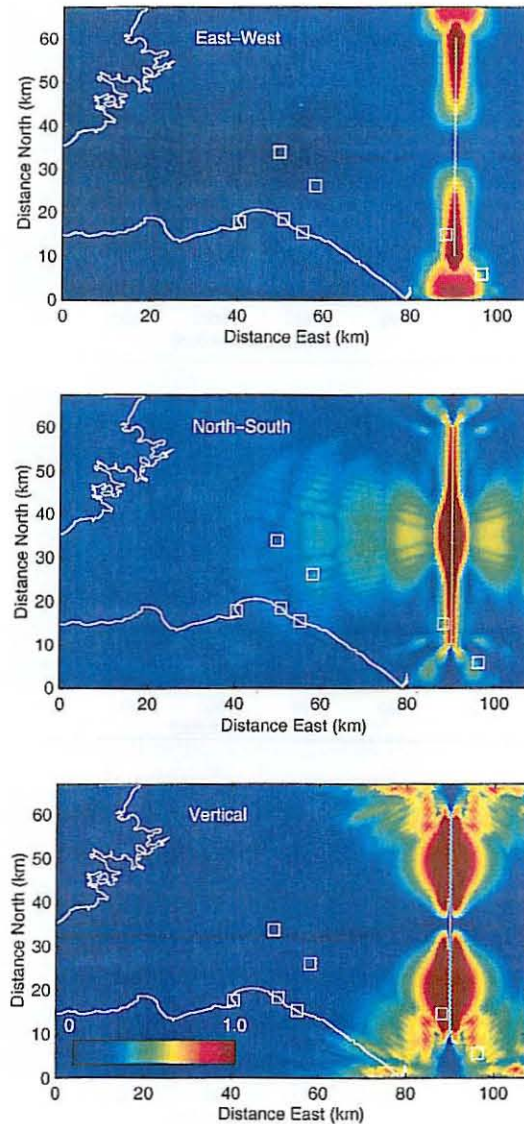


Figure 16. Normalized peak velocities for uniform moment case with 250 m grid spacing ($f_m \sim 1.5$ Hz). The fault is 50 km long and extends from the surface down to 15 km depth. The hypocenter is in the center of the fault at 10 km depth. The peak velocities are normalized by dividing each component by the maximum value for each component from the 400 m grid model (Figure 5).

assumed hypocenter location of the $M_S=6.7$ event (shown with a black star in the figures). A negative sign of $\Delta\sigma_{CFS}$ implies that a right-lateral fault is less likely to break at this location following the $M_S=7.1$ event. In the case of a 20 km long fault the $\Delta\sigma_{CFS}$ is 4.2 bars at the hypocenter location of the second shock. This is a very large change in CFS and more than ample to trigger the second earthquake. Based on our assumptions for the fault locations, it is therefore more likely that a 20 km long fault could have brought the second fault closer to failure than a 50 km long fault, even with less slip on the short fault than we assume. These results are sensitive to the fault locations we use in our study. If the August 14 earthquake occurred further west, and the August 16 event further south, than we assume in our model, we can not rule out

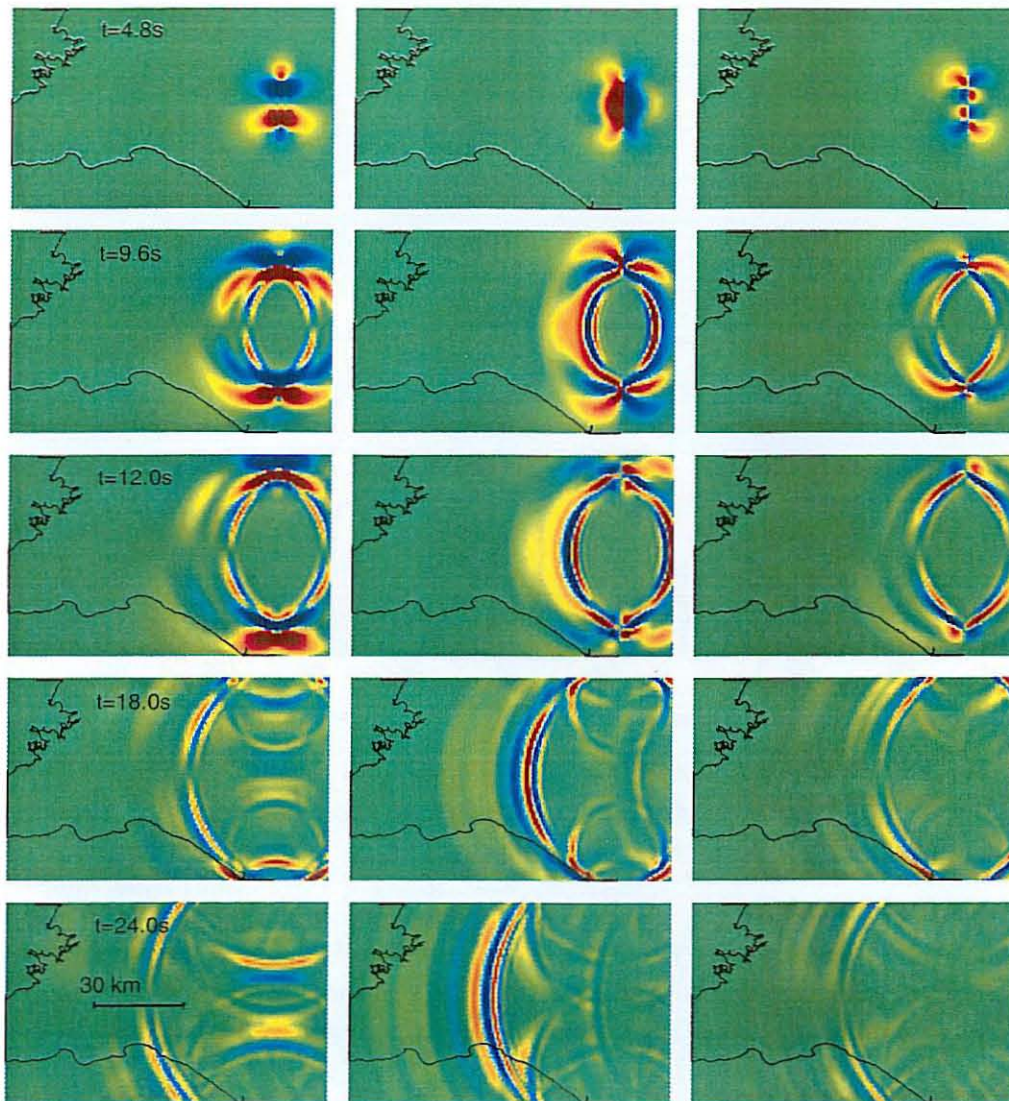


Figure 17. Snapshots of the velocities at times $t = 4.8, 9.6, 12.0, 18.0,$ and 24.0 s in map view for the reference model shown in Figure 4. Red is positive and blue is negative velocity. V_x is fault-perpendicular, V_y is fault-parallel and V_z is vertical velocity. The P-wave amplitudes are so small that they are not seen in the figure. The S-waves can be detected, but the largest amplitudes at times after $t=12$ s are the Love-waves. The S-waves arrive in Reykjavik between 18 and 24 s. Reflections from the boundaries of the model occur after $t=18$ s, but these have lower amplitudes than the peak velocities shown in previous figures.

the possibility of a 50 km long fault triggering the second event.

The pattern of $\Delta\sigma_{CFS}$ close to the fault depends on the slip distribution, but at a distance of 30 km away from the fault the values are similar to what is predicted by uniform slip models with the same moment. Our models do not include viscoelastic rheology, needed to explain the time delay of three days between the earthquakes.

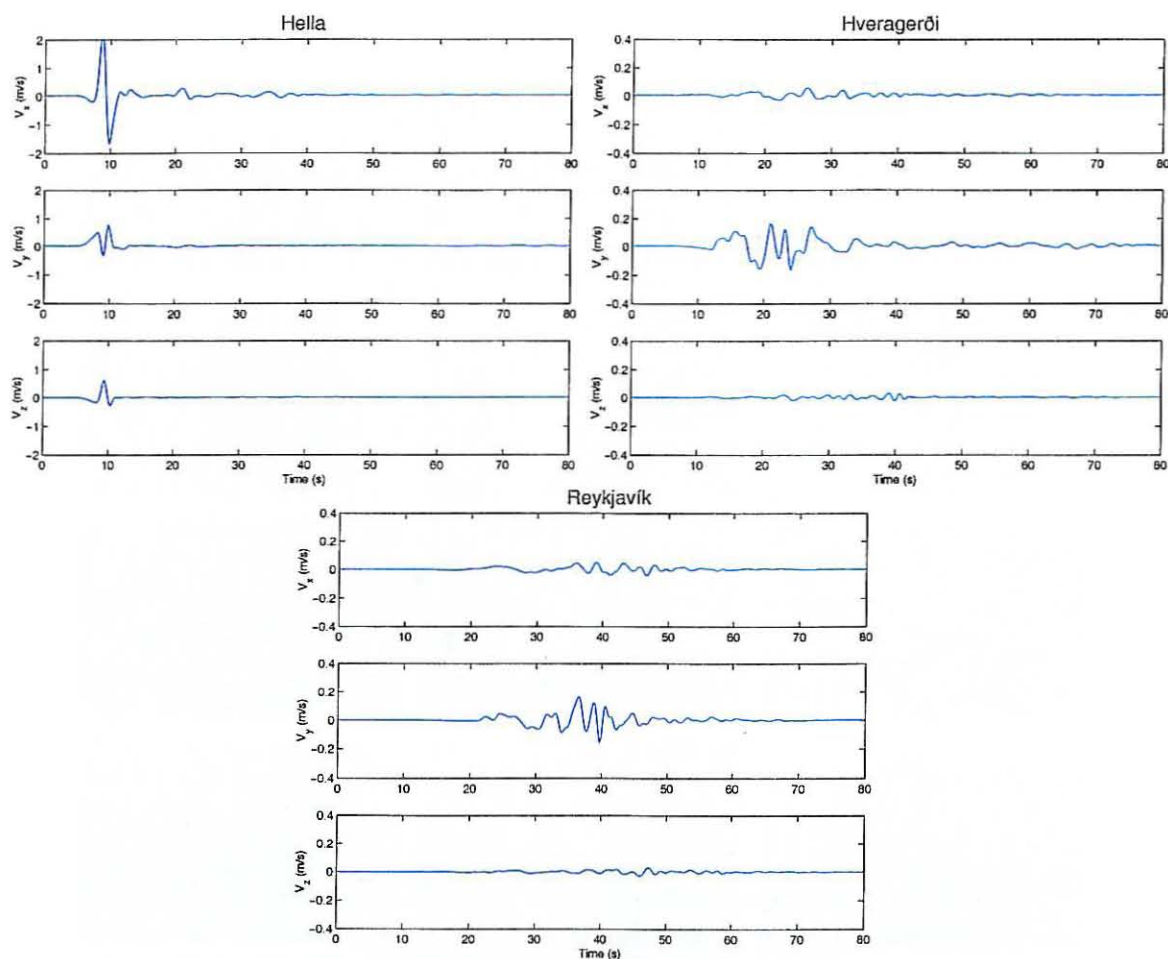


Figure 18. Synthetic seismograms for Hella, Hveragerði, and Reykjavík calculated for the variable slip model shown in Figure 14. V_x , V_y , and V_z are velocities in E–W, N–S, and vertical direction, respectively. The large amplitudes at Hveragerði and Reykjavík are Love-waves. The small bumps in the V_x component at Hella after 12 s are reflections from the southern boundary.

11 DISCUSSION AND CONCLUSIONS

Our study indicates that the predicted surface peak velocities vary considerably between a fault that extends to the surface and a buried fault. The depth to the top of the fault is therefore an important variable in determining accurately the peak surface velocities. Waves generated at shallow depth, where the P-wave velocity increases significantly with depth, are trapped near the surface and generate high surface velocities. In our models this applies down to a depth of 6 km. The mapped surface fractures in the SISZ suggest that the large historical earthquakes ruptured to shallow depths, although they may not have reached the surface along the entire trace of the fault. The slip distribution is also important, particularly the amount of slip at shallow depth. The heterogeneous slip distribution model produces a very different pattern and lower values of peak velocities compared to our reference model. This is probably because the heterogeneous slip model has variable slip at shallow depth. In a large earthquake, such as the $M_S=7.1$, 1784 event, we expect the slip to have been strongly heterogeneous. Uniform moment models will overpredict the peak velocities that we can expect in a large earthquake in the SISZ.

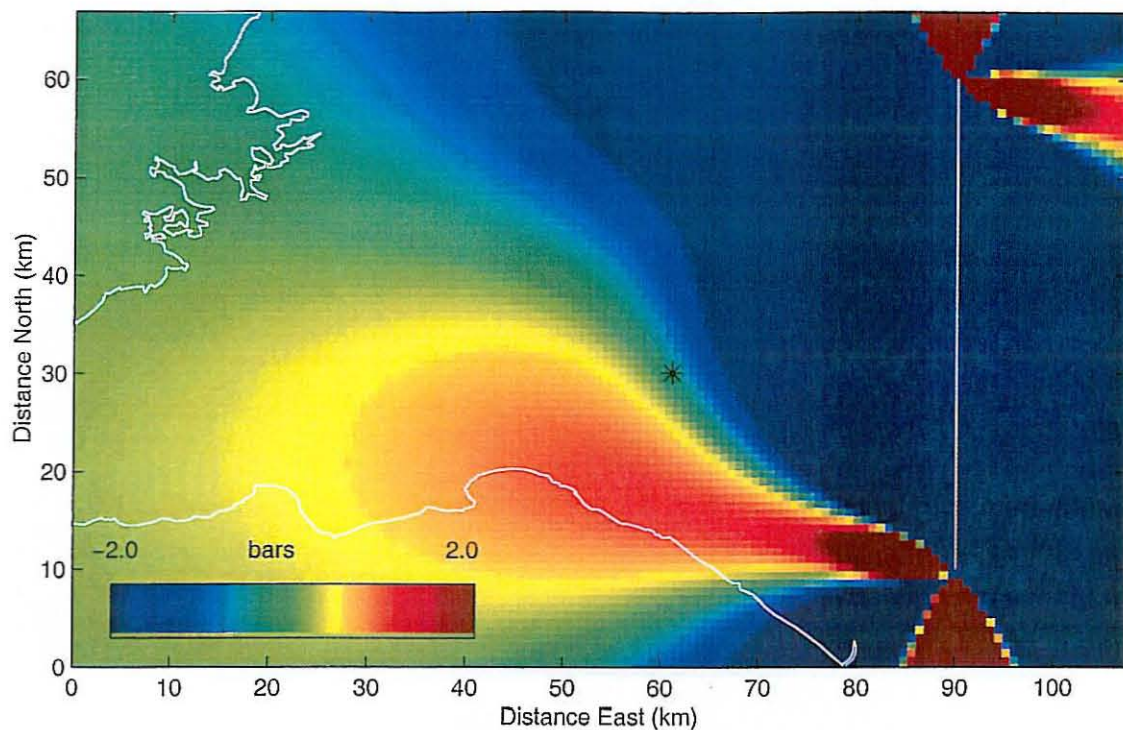


Figure 19. *Coseismic Coulomb stress changes at 5 km depth for a 50 km long uniform slip model, in bars. The black star shows the epicenter location of the $M_S=6.7$, August 16, 1784 earthquake. The coastline and the location of the fault model are shown with white lines.*

These results are in agreement with a study by Graves (1998) based on 3D finite difference simulation of a $M=7.5$ earthquake on the San Andreas fault. He concludes that "... accurate simulation of long period ground motions requires a realistic source parametrization, including appropriate choices of seismic moment and rise time, as well as the use of spatial and temporal variations in slip distribution." In our study we have not examined the effect of changing the seismic moment and rise time. Our simulations with large faults versus small faults demonstrate the effect of changing the slip magnitude, which clearly affects the calculated peak velocities.

We also find increased peak velocities with a higher maximum frequency. The high frequency waves generated in this model would, however, be attenuated if we included anelastic attenuation in our earth model, hence decreasing the peak velocities.

Near the fault, most of the models predict that the maximum velocity occurs in the fault-perpendicular direction, due to the directivity effect. Farther away from the fault, the fault-parallel component (N-S) is larger than the other components. The largest velocities expected in Reykjavík are therefore found on the fault-parallel component for a N-S oriented, vertical, right-lateral slip fault model.

We assume a one dimensional velocity structure for the whole area. Our models would under-

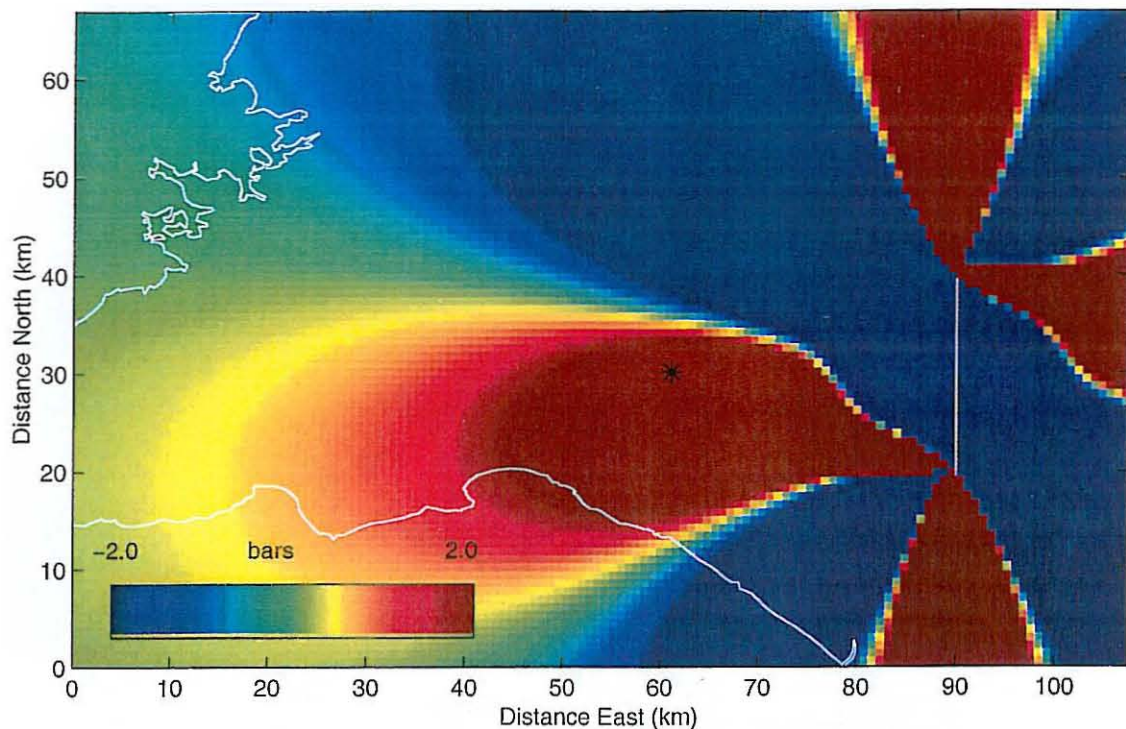


Figure 20. Coseismic Coulomb stress changes at 5 km depth for a 20 km long uniform slip model, in bars. The black star shows the epicenter location of the $M_S=6.7$, August 16, 1784 earthquake. The coastline and the location of the fault model are shown with white lines.

estimate the peak velocities, if basin structures are pronounced in South Iceland.

We calculated the Coulomb stress change for two end member cases, *i.e.*, a short (20 km) fault and a long (50 km) fault. The calculations suggest that if the $M_S=7.1$, August 14, 1784 earthquake ruptured a short fault it is more likely to promote failure at the $M_S=6.7$, August 16, 1784 hypocenter, than a 50 km long fault. This result, however, depends on the relative locations of the faults. The pattern of coseismic Coulomb stress change shows that the first earthquake is likely to have triggered the second earthquake if the southern end of the rupture was due east of the epicenter of the second event. A short fault rupture for the August 14 earthquake agrees with the observations that large historical earthquakes in Iceland generally occur on short faults with anomalously high stress drop (Bjarnason et al. 1993a).

12 ACKNOWLEDGEMENTS

We are grateful to Páll Einarsson, Páll Halldórsson, Ragnar Stefánsson, Sveinbjörn Björnsson, Ingi Þ. Bjarnason, Kristín Jónsdóttir, and Sigurður Th. Rögnvaldsson, who helped us determine the range of reasonable parameters for the simulation and provided other necessary background information on the 1784 earthquakes. Critical review and comments from Kristín S. Vogfjörð and Ingi Þ. Bjarnason greatly improved this report. The figures in this report were generated using the public domain GMT software (Wessel and Smith 1991). The velocity simulations in this study were performed on the SGI Origin 2000 at the Material Research Laboratory,

University of California at Santa Barbara. Financial support for this project was provided in part by the EC project PRENLAB-2 (contract number ENV4-CT97-0536) and the Icelandic Research Council (RANNÍS), grants 981050098 and 981050099 (Þóra Árnadóttir).

13 REFERENCES

- Ágústsson, K., A.T. Linde, R. Stefánsson and S. Sacks 1999. Strain changes for the 1987 Vatnafjöll earthquake in South Iceland and possible magmatic triggering. *J. Geophys. Res.* 104, 1151–1161.
- Árnadóttir, Þ., S.Th. Rögnvaldsson, K. Ágústsson, R. Stefánsson, S. Hreinsdóttir, K.S. Vogfjörð and G. Þorbergsson 1999. Seismic swarms and surface deformation in the Hengill area, SW Iceland. *Seismol. Res. Lett.* 70, 269.
- Árnadóttir, Þ., H. Geirsson, B.H. Bergsson and C. Völksen 2000. The Icelandic continuous GPS network – ISGPS, March 18, 1999 – February 20, 2000. *Rit Veðurstofu Íslands VÍ-R00002-JA02*. Research report, Icelandic Meteorological Office, Reykjavík, 36 pp.
- Bjarnason, I.Þ., and P. Einarsson 1991. Source mechanism of the 1987 Vatnafjöll earthquake in South Iceland. *J. Geophys. Res.* 96, 4313–4324.
- Bjarnason, I.Þ., P. Cowie, M.H. Anders, L. Seeber and C.H. Scholz 1993a. The 1912 Iceland earthquake rupture: growth and development of a nascent transform system. *Bull. Seism. Soc. Am.* 83, 416–435.
- Bjarnason, I.Þ., W. Menke, Ó.G. Flóvenz and D. Caress 1993b. Tomographic image of the mid-Atlantic plate boundary in southwestern Iceland. *J. Geophys. Res.* 98, 6607–6622.
- Björnsson, S. 1978. *Large earthquakes in South Iceland* (Jarðskjálftar á Suðurlandi). Report and maps of a working group to the Civil Defense of Iceland (in Icelandic), 54 pp.
- Cerjan, C., D. Kosloff, R. Kosloff and M. Reshef 1985. A nonreflecting boundary condition for discrete acoustic and elastic wave equations. *Geophysics* 50, 705–708.
- Clayton, R. and B. Engquist 1977. Absorbing boundary conditions for acoustic and elastic wave equations. *Bull. Seism. Soc. Am.* 71, 1529–1540.
- Einarsson, P., S. Björnsson, G. Foulger, R. Stefánsson and Þ. Skaftadóttir 1981. Seismicity pattern in the South Iceland seismic zone. In: D.W. Simpson and P.G. Richards (editors), *Earthquake prediction – an international review. Maurice Ewing Series 4*, Am. Geophys. Union, Washington D.C., 141–151.
- Einarsson, P. and J. Eiríksson 1982. Earthquake fractures in the districts Land and Rangárvellir in the South Iceland seismic zone. *Jökull* 32, 113–120.
- Einarsson, P. and K. Sæmundsson 1987. Earthquake epicenters 1982–1985 and volcanic systems in Iceland. In: Þ.I. Sigfússon (editor), *Í hlutarins eðli*. Map accompanying festschrift for Þorbjörn Sigurgeirsson. Menningarsjóður, Reykjavík.
- Erlendsson, P. and P. Einarsson 1996. The Hvalhnúkur fault, a strike-slip fault mapped within the Reykjanes peninsula oblique rift, Iceland. In: B. Þorkelsson (editor), *Seismology in Europe*. Papers presented at the XXV ESC General Assembly, Reykjavík, Iceland, September 9–14, 1996, 498–505.
- Graves, R.W. 1998. Three-dimensional finite-difference modeling of the San Andreas fault: Source parametrization and ground motion levels. *Bull. Seism. Soc. Am.* 88, 881–897.
- Halldórsson, P., R. Stefánsson, P. Einarsson and S. Björnsson 1984. *Earthquake risk: Dysnes, Geldinganes, Helguvík, Vatnsleysuvík, Vogastapi and Þorlákshöfn* (Mat á jarðskjálftahættu: Dysnes, Geldinganes, Helguvík, Vatnsleysuvík, Vogastapi og Þorlákshöfn). Technical report for the committee for selecting locations for industrial sites. Icelandic Meteorological Office, and Science Institute, University of Iceland (in Icelandic), 34 pp.
- Harris, R. 1998. Introduction to special section: Stress triggers, stress shadows, and implications

- for seismic hazard. *J. Geophys. Res.* 103, 24347–24358.
- Hreinsdóttir, S., P. Einarsson and F. Sigmundsson 2000. Crustal deformation at the oblique spreading Reykjanes peninsula, SW Iceland: GPS measurements from 1993 to 1998. *J. Geophys. Res.*, submitted.
- Jónsdóttir, K., P. Einarsson and V. Hjörleifsdóttir 1999. Surface ruptures of the 1630 and 1784 South Iceland earthquakes (Sprungukerfi Suðurlandsskjálftanna 1630 og 1784). Geoscience Society of Iceland, Spring meeting (in Icelandic).
- King, G., R. Stein and J. Lin 1994. Static stress changes and the triggering of earthquakes. *Bull. Seism. Soc. Am.* 84, 935–953.
- Lay, T. and T.C. Wallace 1995. *Modern global seismology*. Academic Press, San Diego, 521 pp.
- Olsen, K.B. 1994. *Simulation of three dimensional wave propagation in the Salt Lake basin*. Ph.D. thesis, University of Utah, Salt Lake City, Utah, 157 pp.
- Olsen, K.B., J.C. Pechmann and G.T. Schuster 1995. Simulation of 3D elastic wave propagation in the Salt Lake basin. *Bull. Seism. Soc. Am.* 85, 1688–1710.
- Rögnvaldsson, S.Th., Þ. Árnadóttir, K. Ágústsson, Þ. Skaftadóttir, G.B. Guðmundsson, G. Björnsson, K.S. Vogfjörð, R. Stefánsson, R. Böðvarsson, R. Slunga, S.S. Jakobsdóttir, B. Þorbjarnardóttir, P. Erlendsson, B.H. Bergsson, S. Ragnarsson, P. Halldórsson, B. Þorkelsson and M. Ásgeirsdóttir 1998. An earthquake swarm in Ölfus in November 1998 (Skjálftahrina í Ölfusi í nóvember 1998). *Greinargerð Veðurstofu Íslands VÍ-G98046-JA09*. Report, Icelandic Meteorological Office, Reykjavík (in Icelandic), 19 pp.
- Stefánsson, R., R. Böðvarsson, R. Slunga, P. Einarsson, S.S. Jakobsdóttir, H. Bungum, S. Gregersen, J. Havskov, J. Hjelm and H. Korhonen 1993. Earthquake prediction research in the South Iceland seismic zone and the SIL project. *Bull. Seism. Soc. Am.* 83, 696–716.
- Stein, R. 1999. The role of stress transfer in earthquake occurrence. *Nature* 402, 605–609.
- Thoroddsen, Þ. 1899 and 1905. *Earthquakes in Iceland* (Landskjálftar á Íslandi). Hið íslenska bókmenntafélag, Copenhagen (in Icelandic), 269 pp.
- Tryggvason, A., S.Th. Rögnvaldsson and Ó.G. Flóvenz 2000. Three-dimensional imaging of the P- and S-wave velocity structure and earthquake locations beneath Southwest Iceland. *J. Geophys. Res.*, in press.
- Wald, D.J. and T.H. Heaton 1994. Spatial and temporal distribution of slip for the 1992 Landers, California earthquake. *Bull. Seism. Soc. Am.* 84, 668–691.
- Wessel, P. and W.H.F. Smith 1991. Free software helps map and display data. *EOS, Trans. Am. Geophys. Un.* 72, 441 and 445–446.

ISSN 1025-0565
ISBN 9979-878-18-5

Kápmmynd: Klósigar (vatnslær)
Ljós.: Guðmundur Hafsteinsson, veðurfræðingur